Thermodynamic Impact of the Heated Landmass on the Nocturnal Evolution of a Cloud Cluster over a Meiyu-Baiu Front

Hiroyuki YAMADA, Biao GENG

Institute of Observational Research for Global Change (IORGC), Japan Agency for Marine-Earth Science and Technology (JAMSTEC), Yokosuka, Japan

Hiroshi UYEDA

Hydrospheric Atmospheric Research Center, Nagoya University, Nagoya, Japan
IORGC, JAMSTEC, Yokosuka, Japan

and

Kazuhisa TSUBOKI

Hydrospheric Atmospheric Research Center, Nagoya University, Nagoya, Japan
Frontier Research Center for Global Change, JAMSTEC, Yokohama, Japan

Abstract

Numerical simulations of a cloud cluster over a Meiyu-Baiu front were conducted using a cloud-resolving non-hydrostatic model. The purpose was to demonstrate thermodynamic impact of the diurnal heating of the mainland China upon the nocturnal evolution of the cluster. Simulations were conducted within a domain covering eastern and southern China to reproduce land-surface heating on the southern side of the front. The case simulated was a rainband associated with the cluster, which formed on the late afternoon of 22 June 2003. The environment is characterized by a synoptic-scale southerly inflow of warm and moist air in the lower troposphere. A control simulation reproduced the rainband successfully, and showed that the evolution resulted from the strong latent instability over the frontal convergence zone, due to the southerly inflow of the warm and moist air. The origin of this air was the surface heat flux over a cloud-free area to the south of the front. The importance of the heating was proved by a sensitivity simulation without insolation, which failed to reproduce deep convective updrafts. The water budget analysis demonstrated that the evaporation from the ground, rather than the moisture convergence, contributed to the increase in the precipitable water before the rainband evolution. This study, thus, indicates that the continental surface, heated by insolation, has a significant impact upon the nocturnal evolution of a cloud cluster over a Meiyu-Baiu front.

1. Introduction

It is well known that deep convective cloud systems usually develop over a seasonal front in East Asia, referred to as a "Meiyu" or "Baiu" front (hereafter, the Meiyu front). These clouds are sometimes identified as an oval or leaf-shaped cloud shield with a diameter of several

Corresponding author: Hiroyuki Yamada, IORGC, JAMSTEC, 2-15 Natsushima-cho, Yokosuka 237-0061, Japan.
E-mail: yamada@jamstec.go.jp

hundred kilometers in a satellite infrared image. This characteristic shield shape is referred to as a cloud cluster. Since convective cloud systems sometimes cause local heavy rainfall, intensive field experiments, using Doppler radars, have been made since the late of 1980s to clarify the mesoscale structure and environment of the cloud systems.

A common feature of the environment favorable for cloud systems over a Meiyu front is a strong southerly inflow of warm and moist air [i.e., air of high equivalent potential temperature (θ_e)] in the lower troposphere. The low-level horizontal advection of high-θ_e air may destabilize the thermodynamic stratification (i.e., cause latent instability) over the front. A deep convective updraft can form when the high-θ_e air is uplifted to the level of free convection (LFC) by uplifting force over the front. This environmental feature has been described in many studies, based on regional mesoscale observations in East Asia, including Western Japan (Ishihara et al. 1995), the Taiwan Straits (Li et al. 1997), the Korean Peninsula (Shin and Lee 2005), and the Yangtze River basin (Yamada et al. 2003; Geng et al. 2004). The importance of the inflow of warm and moist air in the lower troposphere has also been supported by many numerical simulations (Chen 1991; Kato 1998; Chen et al. 1998; Moteki et al. 2004; Maesaka and Uyeda 2006a). The statistical relationship between the low-level jet and heavy rainfall over northern Taiwan is examined in Chen et al. (2005).

Although the importance of high-θ_e air for the cloud evolution has been pointed out, its source is not sufficiently understood. An analysis of the synoptic-scale moisture balance (Ninomiya and Kobayashi 1992) showed that moisture in East Asia during the 1991 Meiyu period was mainly transported from a tropical area where a monsoon trough formed between westerly and easterly winds. They suggested that the magnitude of the northward moisture flux was the key factor to determine precipitation in East Asia. Since the monsoon trough region itself was not a moisture source (Ninomiya 1999), the Pacific and Indian Oceans seem to have been the major source of the 1991 Meiyu rainfall. Water budget analysis during the 1998 Meiyu season (Hu and Ding 2006) also showed the importance of moisture

transport from the tropical oceans. While the large-scale moisture transport has been examined, however, the local process of the water cycle near the frontal zone is poorly understood. Over mainland China, a Meiyu front, located along the Yangtze River basin, is about 1000 km away from the southern coastline. It is quite likely that local circulation over the landmass modifies the moisture transport process.

Recently, Shinoda and Uyeda (2002) pointed out the importance of paddy fields over mainland China, with regard to the formation of a warm and moist layer in the lower troposphere. Paddy fields distribute widely in the plains of eastern and southern China, and they can supply water vapor to the atmosphere through the latent heat flux. Although this process is not important over a cloudy frontal zone, due to the lack of solar radiation, warm and moist air may form in the daytime over a cloud-free area to the south of the front. This air can be transported northerly to the front by a low-level southerly jet. In a study by Shinoda et al. (2005), using colored moisture analysis, 15% of the total precipitable water in the warm sector of the Meiyu front, originated from the paddy fields. A water budget analysis by Hu and Ding (2006) also referred to the impact of local evaporation, although it was calculated from the residual of the budget equation. Although the contribution of vapor from the continental surface was smaller than that from the oceans (about 67%, according to Table 2 of Shinoda et al. 2005), however, what must not be forgotten here is a thermodynamic importance for initiating deep convection. The accumulation of moisture in the lower troposphere may increase θ_e and cause latent instability. The importance of latent instability for the evolution of cloud clusters over a Meiyu front, is emphasized by Yamasaki (2002), and Yamasaki (2005). A recent study (Li et al. 2007) attempts to relate the surface heating with the strength of the low-level southerly jet. However, no study has attempted to clarify the thermodynamic importance of diurnal surface heating for the evolution of a deep convective cloud system over the front.

In the present study, numerical simulations of a deep convective cloud system over a Meiyu front were conducted using a cloud-resolving

non-hydrostatic model. The objective was to demonstrate the impact of mainland China, heated by insolation, upon the evolution of the frontal convective systems. The case simulated in this study is a cloud cluster that developed over the plains north of the Yangtze River in the late afternoon of 22 June 2003. This cluster was characterized not only by its large and long-lasting cloud shield, such as the mesoscale convective complex (MCC), but also by nocturnal evolution, similar to the global population of MCCs (Laing and Fritsch 1997). The overview of the cluster evolution is described in Section 3, using data collected from an intensive field experiment over the Yangtze River basin, as well as satellite and reanalysis datasets. Using model results, Section 4 describes the process of the formation of high-θ_e air, and the evolution of a rainband corresponding to the cluster. The reproducibility of the simulations is examined on the basis of the observational evidence. In Section 5, the importance of moisture, evaporated from a heated continental surface, is demonstrated by a sensitivity experiment without solar radiation, which can exclude the effect of surface heating. The relative importance of the land-surface moisture supply and synoptic-scale moisture convergence for the rainband evolution is quantitatively examined using water budget analysis (Section 6). The importance of surface heating for the rainband evolution is represented schematically in Section 7, and summarized in Section 8. Throughout this study, local standard time (LST: UTC+8) is used to represent the evolution with time because diurnal variation is an important factor.

2. Model and observation

A non-hydrostatic cloud-resolving model was used in this study, to reproduce the evolution of a convective rainband associated with the cloud cluster, while the observational data were used to show the mesoscale feature of the rainband, and to examine the reality of simulation results. The details of the model and observational data are described here.

a. Model description

The numerical model used here is the Nagoya University Cloud Resolving Storm Simulator (CReSS, version 2.2, Tsuboki and Sakakibara 2002), formulated on the basis of the non-hydrostatic and compressible equation system with terrain-following coordinates. The prognostic variables are three-dimensional velocity components, perturbations of pressure and potential temperature, subgrid-scale turbulent kinetic energy (TKE), and cloud physical variables. The cloud physics is explicitly formulated by a bulk method of cold rain, with variables of mixing ratios and number densities of water substances (i.e., cloud water, raindrops, cloud ice, snowflakes, and graupel particles). Any convective parameterization scheme is not included. Radiation processes are based on the scheme used in the Japan Spectral Model (Segami et al. 1989), which considers the heat balance of the ground surface. The turbulence is parameterized by the 1.5 order closure with TKE. More details are provided in Wang et al. (2005).

A control simulation was conducted within doubly nested domains, with horizontal grid spacing of 5 km (coarse mesh), and 2 km (fine mesh). The coarse mesh domain consists of 540×370 grids in the horizontal domain, and covers a 2,700 km $\times$ 1,850 km area, while the fine mesh consists of 500×400 points, covering an area of 1000 km $\times$ 800 km. The topography in and around the model domains, shown in Fig. 1, indicates that the coarse-mesh grids cover the plains and hills in eastern and southern China. The vertical grids consist of 50 levels, with an interval that stretches from 100 meter (near sea surface) and 372 meter (near the top: 14.8 km ASL). Grids under the ground (for representing the soil temperature) consist of 40 levels. A sensitivity experiment, without insolation, was performed within the same nested domains as the control simulation. These simulations were performed by the NEC SX-5 and the SX-8 of the Japan Agency for Marine-Earth Science and Technology (JAMSTEC).

The numerical experiments were conducted for 24 hours, from the initialization at 0200 LST 22 June 2003. The start of simulations from four hours before sunrise was aimed to reproduce the diurnal heating of surface and boundary layer, preceding the rainband evolution. The initial fields and lateral boundary conditions of the model were given using the six-hourly regional objective analysis dataset,
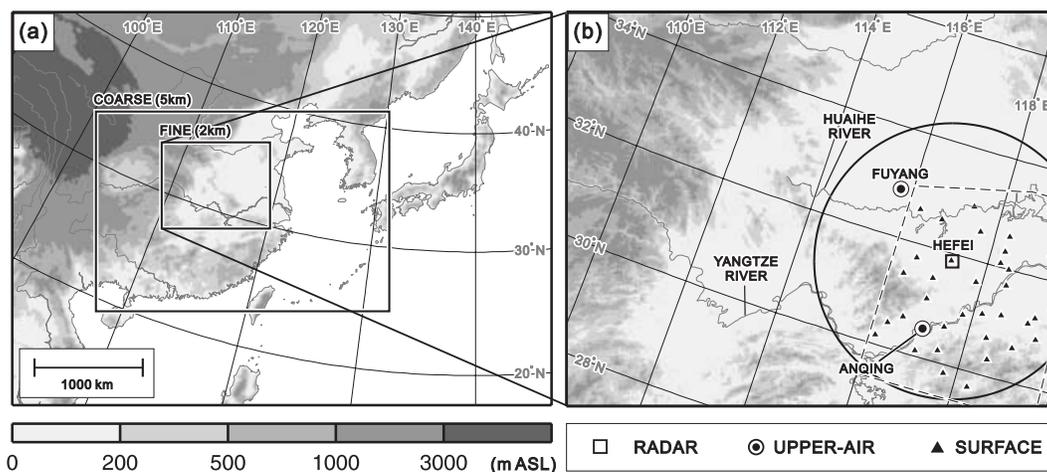
Fig. 1. (a) Topography in and around the model domain. Two rectangles show the domain of the coarse and fine mesh models. (b) Topography and location of the radar and weather stations in the fine-mesh model. A circle shows the 280-km range of the Hefei Doppler radar. The area enclosed by a dashed line shows the surface-observational network.

provided by the Japan Meteorological Agency, with horizontal grid spacing of 20 km. The surface temperature over the ocean was obtained from the optimum interpolation sea surface temperature (OISST, Reynolds et al. 2002). The altitude of the land surface were obtained from the real topographic data (the global 30 arc second elevation data: GTOPO30). The land-surface conditions were not obtained from any external dataset but initiated homogeneously by assuming a land use of primarily paddy fields. The surface parameters observed and modeled in the GAME-HUBEX[1] project (Ikebuchi et al. 1998; Shinoda and Uyeda 2002) were taken into account to determine the parameters shown in Table 1. Although the actual land surface is inhomogeneous (because of the presence of several land-use categories), this assumption is roughly appropriate to the present case because the area heated by insolation and supplying sensible and latent heat to the front was limited in the rice-farming plains, between 28 and 33°N.

b. Observational data

This study used the radar reflectivity and upper- and surface-meteorological data, col-

Table 1. Surface parameters used in the simulation.

Albedo	0.2
Evapotranspiration efficiency	0.5
Roughness length $[m]$	0.4 (for wind velocity)
	0.1 (for scalar variables)
Thermal capacity $[10^6\ Jm^{-3}K^{-1}]$	2.3
Thermal diffusivity $[10^{-7}\ m^2s^{-1}]$	7.0

lected within the fine-mesh model domain, by an intensive field experiment under the cooperative project between the JAMSTEC, and the China Heavy Rainfall Experiment and Study (CHeRES). The experiments were conducted every Meiyu season from 2001, and the details are described in Yamada et al. (2003). Since 2003, the target area was concentrated on the area within the coverage of the Hefei S-band Doppler radar (see Fig. 1b), in order to monitor the relationship between the evolution of heavy rainfall and mesoscale flow disturbed by the local topography.

The reflectivity data were collected every 5 minutes by the radar's three-dimensional scan (i.e., volume scan), consisting of 14 elevation steps from 0.2° to 20.0°. Raw data were inter-

---

1 GEWEX Asian Monsoon Experiment/Huaihe River Basin Experiment, GEWEX: Global Energy and Water Cycle Experiment.

polated to a grid volume by the spherical co-ordinates (longitude, latitude, altitude), using a Cressman-type weighted interpolation technique. The grid spacing was $0.02°$ in the two horizontal directions, and 1.0 km in the vertical direction from the lowest plane of 1.0 km above sea level (ASL). The upper-air observations were carried out every 6 hours at the Fuyang and Anqing stations. The surface observation network consisted of 32 stations collecting wind speed and direction, pressure, temperature, dew-point temperature, and rainfall amount every hour. In addition to these data, infrared and visible imageries of the Geostationary Operational Environmental Satellite (GOES-9), were also used.

3. Case overview

The rainband under investigation developed with the evolution of a frontal depression in the late afternoon of 22 June, and maintained in the night. The overall evolution, mesoscale characteristics, and synoptic situations of the rainband are described in the following subsections, using the observational and reanalysis data.

a. Overall evolution

The overall evolution of the rainband and depression can be traced using infrared satellite imagery with a surface weather chart, as shown in Fig. 2. This frontal depression was spawned from a stationary depression in the eastern foot of the Tibetan Plateau (the so-called "southwest vortex" in China) by the afternoon of 22 June (Figs. 2a–c), and then moved north-eastward. The cloud distribution around the depression is characterized by a large λ-shape cloud zone (Figs. 2d–f), consisting of three bands extending north, east, and southwest from the depression center. The cloud pattern is somewhat similar to that shown in Ninomiya (2001) and reflects the strong influence of the synoptic-scale flow, which is described later.

The high-cloud shield (i.e., cloud cluster) of the rainband (marked "CC" in Fig. 2d) appeared in the trailing portion of the depression (i.e., in the southwestern cloud band) after the sunset. The area of cloud-top black-body temperature (T_{BB}) lower than $-70°C$ remained stationary near $115°E$, $32°N$ until the next

morning (Figs. 2d–f). The area of the $-52°C$ cloud shield was 420,000 km^2 at the maximum (at 23 LST), and larger than 50,000 km^2 for 19 hours. The horizontal extent and duration were relatively larger and longer, respectively, than those of cloud clusters during the Meiyu season (according to Iwasaki and Takeda 1993), and satisfied the criteria of MCC and persistent elongated convective systems (PECS) over the United States (Anderson and Arritt 1998).

What must not be overlooked in this figure is the area of high-T_{BB} ($\geq 10°C$) that extended to the south of the frontal depression in the daytime (Figs. 2b–c). The high-cloud shield (CC) was formed just northeast of the high-T_{BB} area. More detailed features of the high-T_{BB} area, and its importance for the evolution of the rainband, are given in the following subsection.

b. Mesoscale characteristics

Changes in the mesoscale characteristics before and after the formation of the high-cloud shield within the radar observational area are shown in Fig. 3. Before the formation (Fig. 3a), the surface depression located near $113°E$, $33°N$. Weak (≤ 40 dBZ) and broad echoes extending to the east of $116°E$ correspond to a weak rainfall area in front of the depression, while the no-echo area in the western part of the radar observational range corresponds to the high-T_{BB} area mentioned above. To confirm the small amount of clouds in the high-T_{BB} area, the area of fine weather was calculated using visible satellite images. In this study, fine weather is defined as the condition under which albedo lower than 0.3 continued longer than 4 hours in 08–16 LST. The distribution of fine weather (superimposed in Fig. 3a) shows that the cloud amount of the no-echo area was certainly low and suggests the surface heating in the daytime. It is noteworthy that an area of equivalent potential temperature higher than 356 K was distributed in the south of the rainfall area. This paper refers to this area as 'high-θ_e' because the past studies (e.g., Chen et al. 1998; Yamada et al. 2003) reported that such value was seen near the surface on the southern side of a Meiyu front prior to the evolution of convective systems. Since the surface wind in the south of
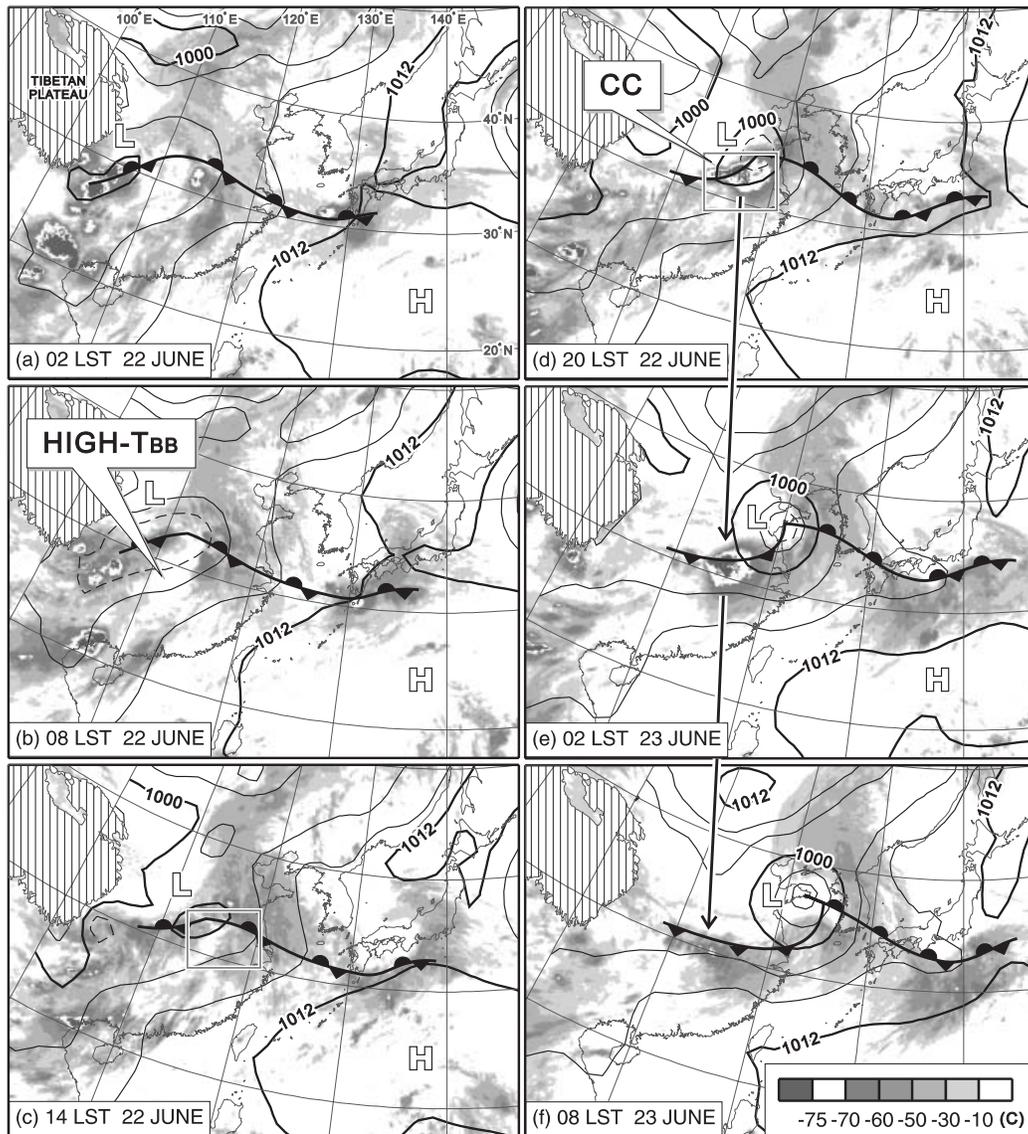
Fig. 2.   Series of cloud-top black-body temperature (T_{BB}) with a surface weather chart every 6 hours between 02 LST 22 June and 08 LST 23 June 2003. The hatched area is the Tibetan Plateau with an altitude higher than 3,000 m ASL. Bold arrows show the location of a cloud cluster (CC) investigated in this study. The rectangles in (c) and (d) are the field experimental area shown in Fig. 3.

the weak rainfall area was southerly, it is suggested that the high-θ_e air may have originated from the fine-weather area distributed to the south of the weak rainfall area.

The reflectivity distribution at 20 LST (Fig. 3b) shows the evolution of a rainband with strong echoes (≥ 45 dBZ) and high-cloud shield. The surface-wind distribution indicates

that this rainband developed over a wind-shear line in the Meiyu frontal zone because the wind direction shifted from southerly to westerly along the rainband. It is noteworthy that high-θ_e air still extended to the south of the rainband.

To describe the duration of the high-θ_e air and its relevance to the rainband evolution,
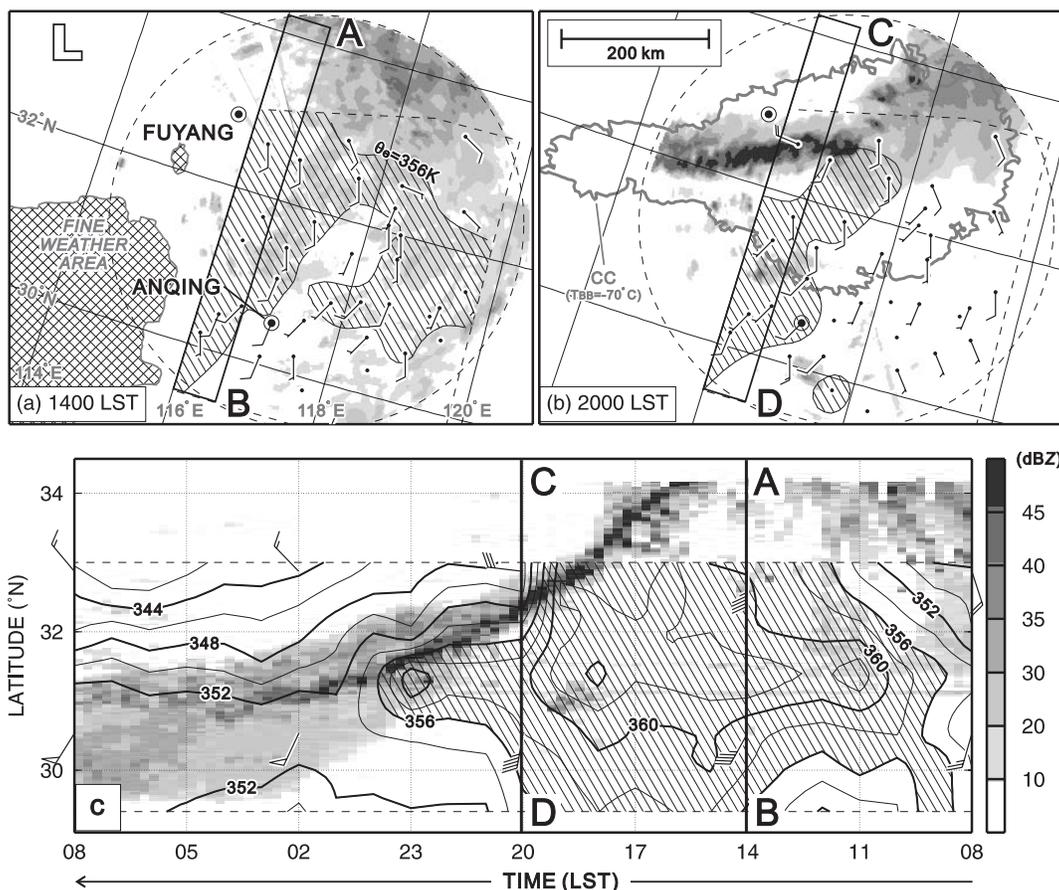
Fig. 3. (a and b) Radar reflectivity at 3.0 km ASL and wind barb at the surface on 1400 and 2000 LST 22 June. Half and full barbs indicate 2 and 4 ms^{-1}, respectively. Shading indicates the area where equivalent potential temperature at the surface level is larger than 356 K. In the panel (a), the mark "L" indicates the center of a frontal depression (shown in Fig. 2c), and the cross-shaded area corresponds to the fine-weather area (defined in the text). In the panel (b), a contour of T_{BB} lower than $-70°$C is superimposed. (c) Time-latitude section of the radar reflectivity at 3.0 km ASL, wind barbs at 950 hPa, and equivalent potential temperature at the surface. The direction of the time axis is toward the left.

time-latitude sections of the reflectivity at 3.0 km ASL, wind barbs at 950 hPa, and θ_e at the surface are shown in Fig. 3c. The reflectivity and θ_e were averaged zonally within 0.5° width; in other words, lines A–B and C–D correspond to the strips in Figs. 3a and b, respectively. This panel clearly shows that the area of southerly wind with high-θ_e air extended from the no-echo (i.e., fine-weather) area to the south of the frontal rainfall area in the daytime, and that this flow remained until midnight. The rainband developed over the area where the southerly high-θ_e air and northwesterly air with surface-level θ_e lower than 348 K

were converged. It is noteworthy that reflectivity higher than 45 dBZ remained in the rainband until the high-θ_e area disappeared. These facts indicate that the southerly high-θ_e air from the fine-weather area closely related to the nocturnal evolution of the rainband.

The vertical thermodynamic features over the high-θ_e area are described using the vertical profile over Fuyang at 14 LST (Fig. 4a). The high-θ_e air ($\geq$356 K) extended below 2 km ASL and caused latently unstable stratification favorable for the evolution of a deep convective updraft. The highest θ_e, which was 362.4 K at 0.2 km ASL, contained a large

Fig. 4. (a) Vertical profile of the vapor mixing ratio (qv), potential temperature (θ), equivalent potential temperature (θ_e), saturated equivalent potential temperature (θ_e^*), and wind barb observed at Fuyang (see Fig. 3) on 14 LST 22 June. A pennant indicates 20 ms^{-1} while barbs are drawn in the same manner as in Fig. 3. (b) Time-height section of equivalent potential temperature and wind barb observed every 6 hours at Fuyang.

amount of vapor (21.7 g kg^{-1} in the mixing ratio) and had the potential to rise to the level of neutral buoyancy (LNB) at 14.0 km ASL after being uplifted to LFC at 1.8 km ASL. The convective available potential energy (CAPE) for the highest θ_e was 1093 m^2 s^{-2}, which increased from 296 m^2 s^{-2} at 08 LST, indicating significant destabilization in the daytime. It is certain that the high-θ_e air was transported northward by the strong southerly jet (with the peak of 23 ms^{-1} at 1.5 km ASL), and formed a deep updraft in the rainband over the front where this air could be uplifted to LFC by horizontal convergence in the lower troposphere. The profile of saturated equivalent potential temperature (θ_e^*) suggests that the air north of the front had no potential to form convective updraft because the lowest value of θ_e^* in the profile (i.e., 352 K at 4.3 km ASL) was higher than the surface-level θ_e to the north of the front ($\leq$348 K, described above), causing no CAPE.

To examine the duration of the high-θ_e-air supply in a timescale longer than that in Fig.

3c, the time-height cross section of θ_e and the horizontal wind barb is shown in Fig. 4b. It is clear that the northward transport of high-θ_e air was limited only in the half-day preceding the evolution of the rainband (marked "CC"). At the model initialization time (02 LST 22 June), θ_e in the lower troposphere ($\leq$2 km ASL) was lower than 350 K.

c. Synoptic situations

Changes in the synoptic-scale conditions from the model initialization time through 18 hours later are described using the reanalysis data (Fig. 5). The distributions of the geopotential height in the middle troposphere (Fig. 5a) clearly show that a westerly trough propagated eastward and deepened rapidly. This trough accompanied the ascent motion on the forward (eastern) side. It is certain that the frontal surface depression developed under the influence of the westerly trough, providing cyclonic vertical vorticity and upward motion (negative value of ω). The zonal contrast of θ_e in this layer became large near the trough

Fig. 5. Changes in the synoptic-scale conditions between 02 LST (left panel) and 20 LST (right panel). A star and bold line in each panel indicate the location of a depression and Meiyu-Baiu front at the surface. (a) Geopotential height (solid contour), equivalent potential temperature (broken contour), and vertical velocity (shades) at 500 hPa. (b) Geopotential height (solid contour) and equivalent potential temperature (contour and shades) at 925 hPa. (c) Vapor flux vectors at 925 hPa and latent stability represented as $(-[\theta_e(925 \text{ hPa}) - \theta_e^*(600 \text{ hPa})]/\Delta p)$, with the unit of $\text{K} \cdot (100 \text{ hPa})^{-1}$.

axis, and reached 16 K in 500 km width (in maximum) on 20 LST. This reflects the large zonal contrasts of moisture (5 g kg^{-1}) and the weak contrast of temperature (2°C), which were caused by the advections of southerly moist air in the forward portion and northwesterly dry air in the rear.

The change in the high-θ_e distribution at 925 hPa is described using Fig. 5b. At 20 LST, an area of θ_e larger than 352 K extended to

the southwest of the depression center. This area has clearly become much wider than that at 02 LST. A marked change is also seen in the distributions of latent stability (Fig. 5c) estimated between 925 and 600 hPa. The increase in the area of negative value over the continent indicates that the area of latent instability was widen in the daytime. The low-level synoptic flow over the continent is characterized by the southerly inflow to the Meiyu

front. This evidence suggests that the heating of the low-level southerly inflow over the continent in the daytime was responsible for the rapid extension of the areas of high-θ_e and the latent instability.

4. Model results

In the previous section, observational evidence suggests that the formation of the high-θ_e air in the daytime was a key of the nocturnal evolution of the rainband. The descriptions in this section, therefore, address the origin of the high-θ_e air and its effect on the rainband evolution, as well as the reproducibility of model results through comparisons with the observational and reanalysis data.

The overall features of the results of the coarse-mesh control simulation are shown in Fig. 6. The sea-level pressure distributions (Fig. 6a) show that the frontal depression de-
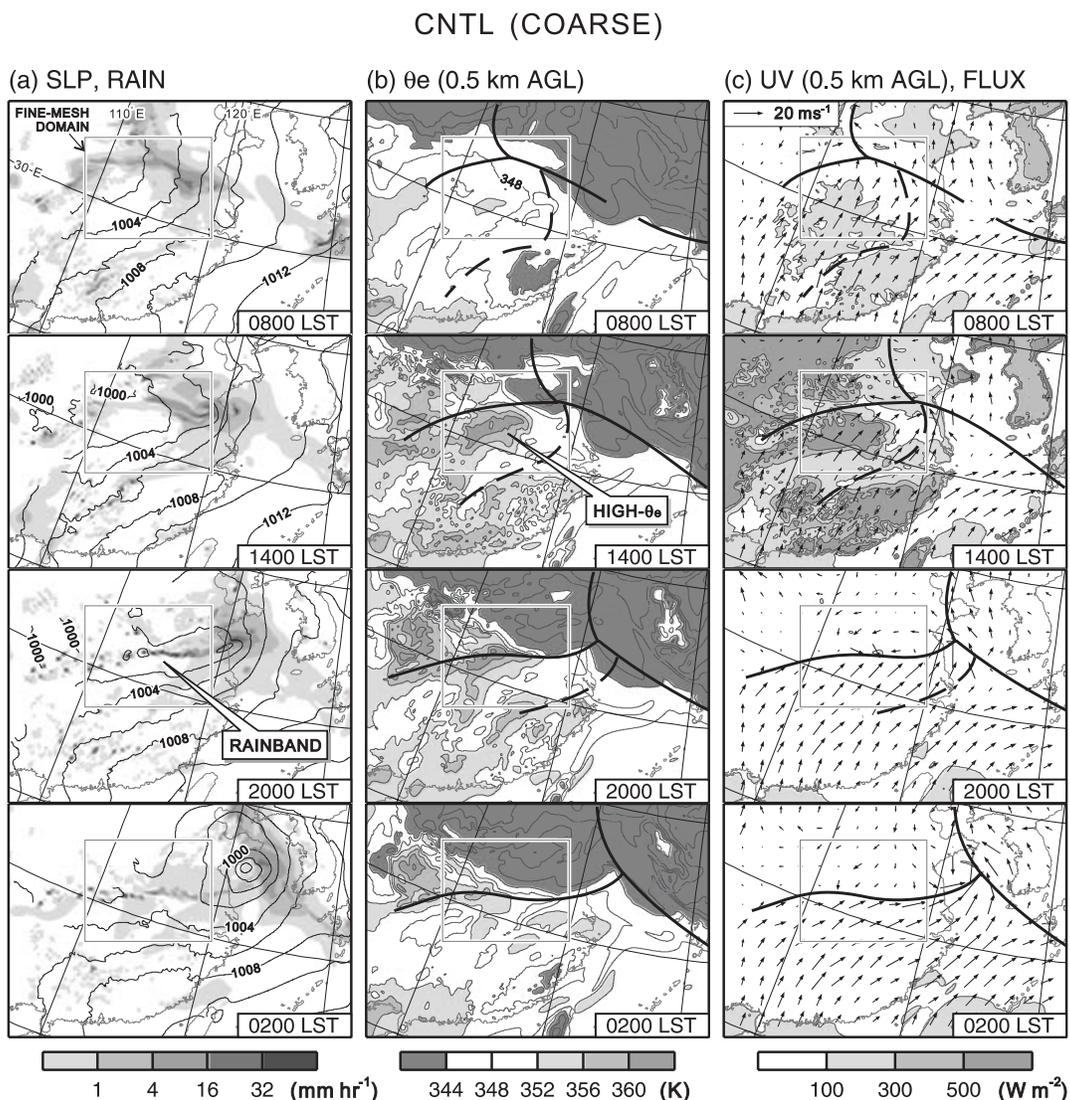

Fig. 6. Horizontal distributions of the coarse-mesh control experiment. (a) Rainfall intensity at the surface (shade) and sea level pressure (hPa, contour). Pressure contours are drawn in areas where the surface altitude is lower than 500 m ASL. (b) Equivalent potential temperature at 0.5 km above the ground level. (c) Wind vector at 0.5 km above the ground and sum of the sensible and latent heat fluxes at the surface level.

CNTL (FINE)
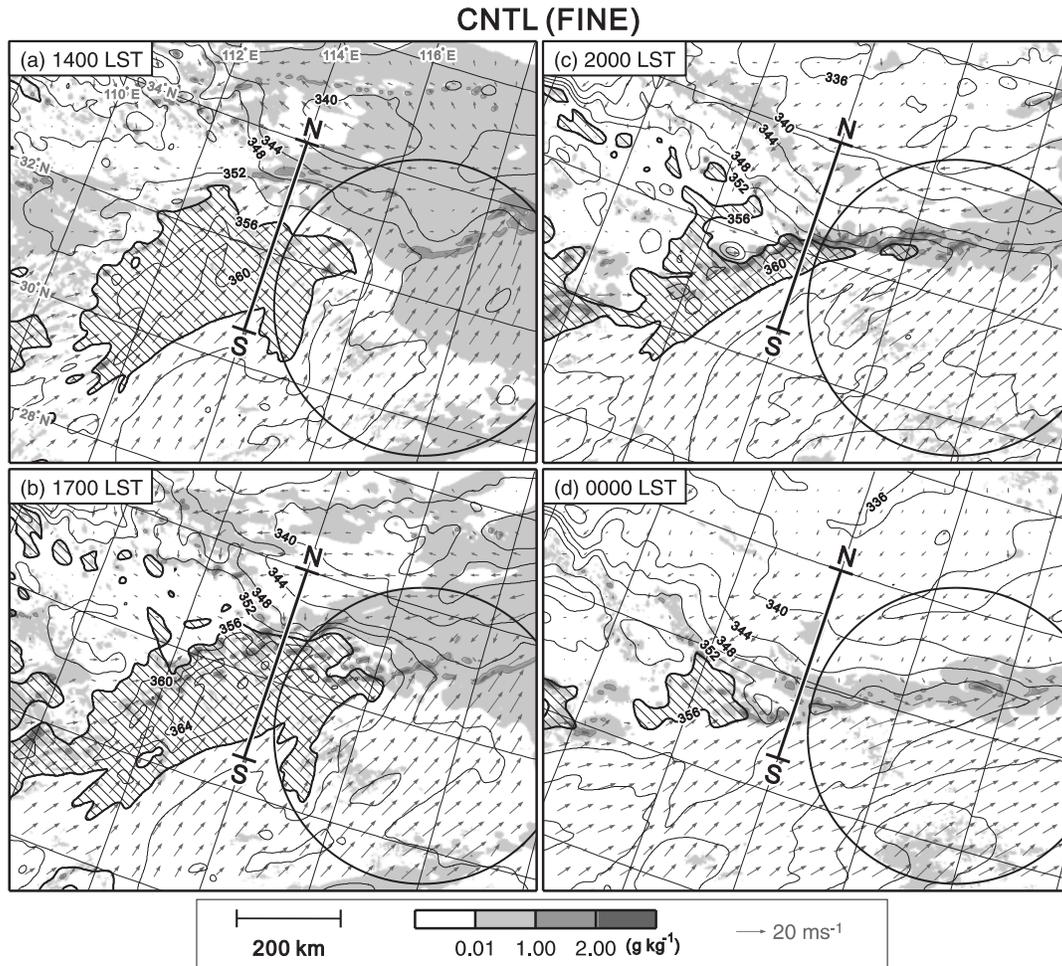
Fig. 7. Horizontal distributions of the hydrometeor mixing ratio (shade), θ_e (contour), and wind vec-
tor of the fine-mesh control experiment at 0.5 km above the ground level. Areas of θ_e higher than
356 K are hatched and surrounded with a bold line.

veloped and reached near the east coast at
0200 LST of the next day. The reproducibility
of the location and pressure of the depression
center is roughly good, as compared to Fig. 2e.
The rainfall distributions show that the model
reproduced two types of major rainfall areas:
wide and weak rain near the depression cen-
ter, and a narrow band of strong rainfall (i.e.,
convective rainband) in the trailing portion of
the depression. The reality of the rainfall pat-
tern is discussed later using the fine-mesh
model results. The distributions of both θ_e (Fig.
6b) and the moisture flux (Fig. 6c) at 2000
LST resemble those from the reanalysis data
(right panel of Figs. 5b and c, respectively).

That is, southerly inflow of high-θ_e air to the
south of the convective rainband was repro-
duced well.

A noteworthy point in this figure is the large
dependence of the θ_e distribution on the rain-
fall pattern. Most areas higher than 356 K be-
gan to appear rapidly by 1400 LST out of the
rainfall areas (marked by bold lines), and grad-
ually disappeared in the night. In particular,
the high-θ_e area near 113°E, 31°N, at 1400 LST
(highlighted by a balloon), corresponds to the
high-T_{BB} area (shown in Fig. 2). The distribu-
tions of the sum of sensible and latent fluxes
at the surface (Fig. 6c) show that areas with
large flux (at 1400 LST) corresponded to the

high-θ_e areas. This suggests that high-θ_e air was formed by the heat and moisture supply from the continental surface in the daytime.

To describe the detailed rainfall distribution of the rainband and its relation to the high-θ_e area, the horizontal distributions of the fine-mesh control simulation result are shown in Fig. 7. The high-θ_e area (shaded) was formed by 1400 LST within the southerly-inflow area to the southwest of the wide and weak rainfall area. At 1700 LST (Fig. 7b), the convective rainband, consisting of rainfall cores (i.e., those with a mixing ratio larger than 2.0 g kg^{-1}), began to organize along the northern edge of the southerly inflow (i.e., in the frontal zone). Individual rainfall cores developed near the northern edge of the high-θ_e area, and moved at about 11 ms^{-1} east-northeasterly along the rainband. Such evolution of the rainband remained until the high-θ_e area almost dissipated (Fig. 7d). During the evolution, northerly inflow on the northern side of the rainband was reinforced near the rainfall cores (e.g., 114–115°E, 33°N, in Fig. 7c). The model results indicate good qualitative correspondences with the observed evidence in the following points. The distributions of the water substance mixing ratio within the radar circle at 1400 and 2000 LST resemble to those of reflectivity pattern (Figs. 3a and b), that is, the wide and weak rainfall area in the daytime and the rainband in the night were reproduced well. The distributions of the high-θ_e area at 1400 and 2000 LST were also roughly comparable to the observed distributions (Figs. 3a and b).

To examine the origin of air parcels, taken into the updrafts of the convective rainband, the trajectory of air parcels is shown in Fig. 8. Four parcels were selected from strong updraft regions ($\geq$5.0 ms^{-1}) at 5.0 km ASL on 20 LST, and were traced forward and backward using the results of the fine-mesh control experiment. All of these parcels came from the southern side of the rainband, and passed in the layer near the surface in the daytime. It is noteworthy that the parcels moved within the area of high-θ_e, which indicates high-θ_e air having been taken into the convective rainband.

The detailed process of the rainband evolution is described using the vertical sections of the hydrometeor mixing ratio and θ_e (Fig. 9) and airflow (Fig. 10) along the S–N line
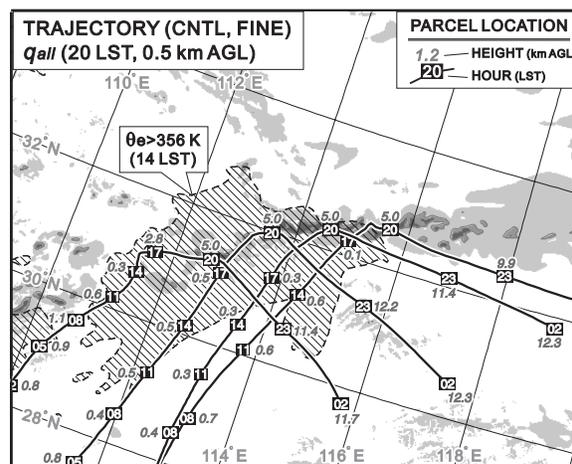
Fig. 8. Trajectory analysis using the results of the fine-mesh control experiment. Four parcels in strong updraft regions ($\geq$5.0 ms^{-1}) at 5.0 km ASL on 20 LST were selected as the initial location and traced forward and backward. Horizontal distributions of the hydrometeor mixing ratio on 20 LST at 0.5 km above the ground level (using the same gray scale as Fig. 7) and the θ_e higher than 356 K on 14 LST at the same vertical plane are also shown.

(shown in Fig. 7). The cloud area is defined here as one enclosed by the 10^{-9} g kg^{-1} contour of hydrometeor mixing ratio. Note that the horizontal axis of Fig. 10 is magnified to show the detailed airflow structure in the vicinity of the front. In both figures, the front between the southerly and northerly winds is depicted by a bold broken line. It is clear, in Fig. 9, that high-θ_e air ($\geq$356 K, marked by a solid bold contour) formed near the surface over the cloud-free area to the south of the cloudy frontal zone by 1400 LST. This air had the depth less than 2 km, moved northward, and approached to the front by 1550 LST. The airflow (Fig. 10) indicates that weak updraft ($\leq$1 ms^{-1}) in the wide and weak rainfall was replaced with a strong one ($\geq$10 ms^{-1}) of the convective rainband after 1550 LST. It is noteworthy that cloud-top height (the top of the 10^{-9} g kg^{-1} contour) increased from 10 (at 1400 LST) through 14 km ASL (by 1700 LST). The strong updraft of the rainband remained at 2000 LST (Fig. 10e), but it began to decline
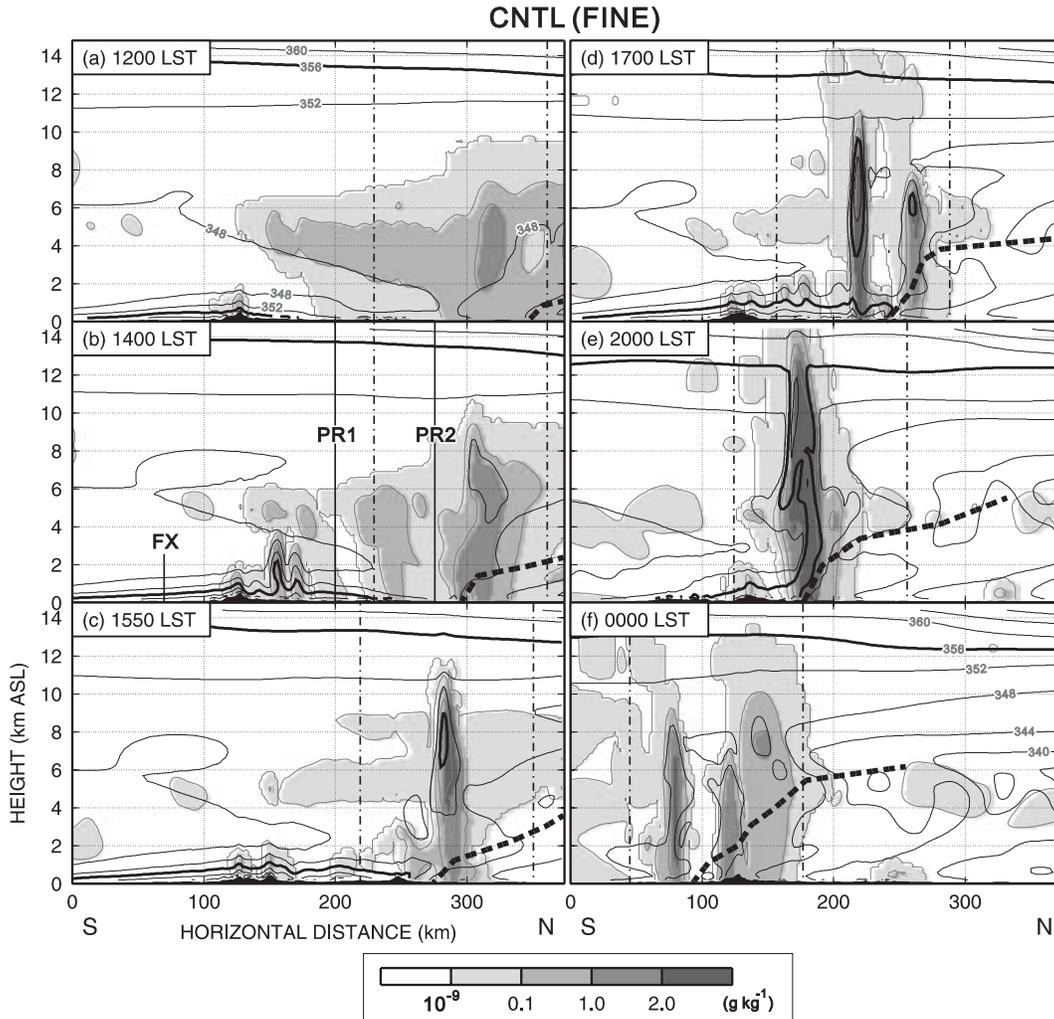
Fig. 9. Vertical sections of the hydrometeor mixing ratio (shade) and θ_e (contour, every 4 K) along S–N line shown in Fig. 7. The contours of 356 K are highlighted with a bold solid line. A bold broken line in each panel shows the wind shear line corresponding to the front. Two dash-dotted lines indicate the border of the area displayed in Fig. 10.

by midnight (Fig. 10f). The θ_e distributions in the evening and nighttime (Figs. 9d–f) show that the area of high-θ_e air reduced its meridional extension, and disappeared by 0000 LST. This result indicates that deep updrafts of the convective rainband was sustained during the period that high-θ_e air was supplied from the south of the front.

The vertical thermodynamic profile over the two points ("PR1" and "PR2," see Fig. 9b) at 1400 LST is shown in Fig. 11. The profile over PR1 shows large latent instability, represented by an area where θ_e^* of each vertical level is

lower than near-surface θ_e (i.e., positive area, shaded in the profile). The CAPE was 1776 m^2 s^{-2}. It is clear that the high-θ_e air near the surface was responsible for this latent instability. In contrast, the profile over PR2 shows very small latent instability with LNB near 10 km at this time. Latent instability, however, can be expected to become large when the near-surface high-θ_e air at PR1 reaches PR2. Using the surface-level θ_e over PR1, the positive area above PR2 may extend greatly, and the LNB may rise from 10 to 14 km ASL. This estimation corresponds to the

CNTL (FINE)
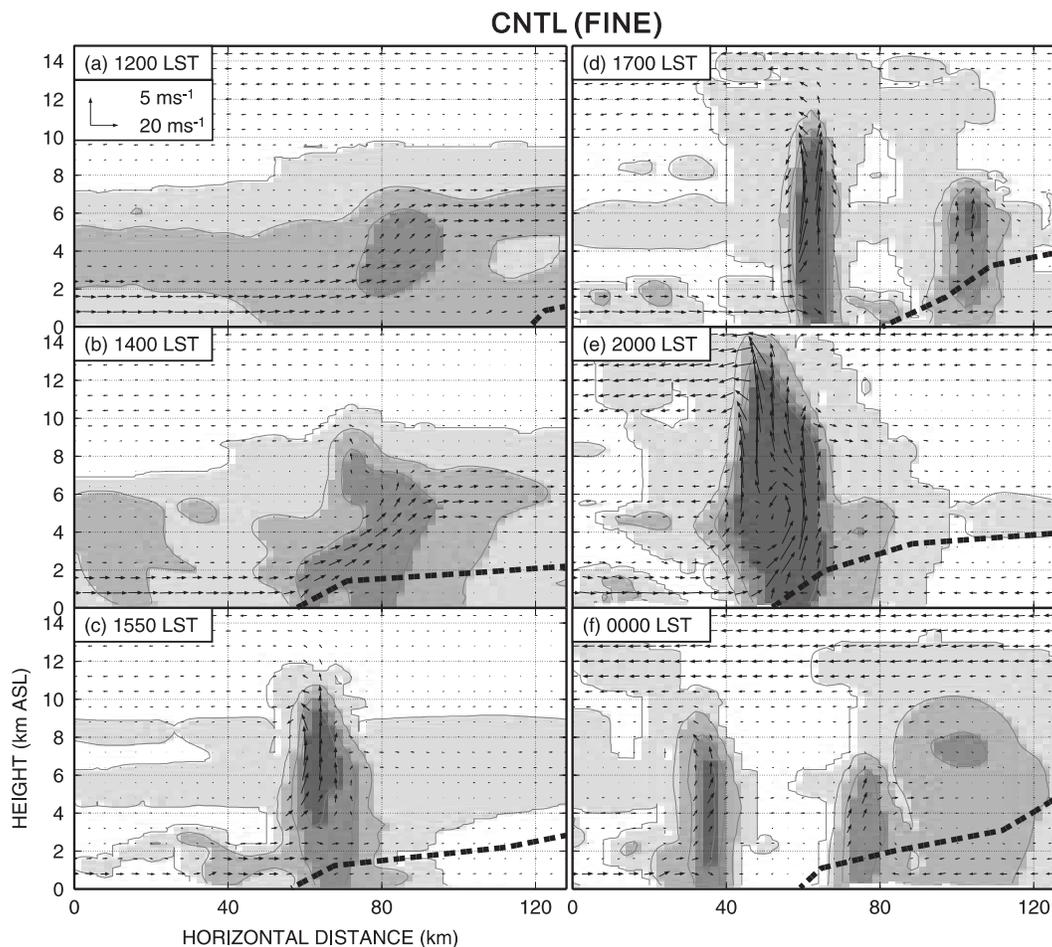
Fig. 10.   Vertical sections of the hydrometeor mixing ratio (shade) and wind vectors along a part of S–N line. Note the horizontal axis is magnified, and the displayed areas are shown in Fig. 9.

increase in the depth of updraft core after the evolution of the rainband (as shown in Figs. 10b and c).

The diurnal variation in the surface heat fluxes in a cloud-free area to the south of the front ("FX" point in Fig. 9b) is shown in Fig. 12. Net shortwave radiation (SR) caused large latent heat flux (LHF) reaching 500 W m^{-2} and small sensible one (SHF) at most 150 W m^{-2}, which were responsible for the increase in the near-surface θ_e in the daytime. The predominance of latent heat resulted from the wet surface conditions (mostly paddy fields). The maximum values of the latent and sensible heat fluxes and net shortwave radiation in the daytime roughly correspond to the results of GAME-HUBEX (Shinoda and Uyeda 2002).

Therefore, in summary, the control simulations reproduced the convective rainband without contradicting the observational evidence. The evolution of the rainband resulted from the strong latent instability over the frontal zone, due to the southerly inflow of the warm and moist air near the surface. The origin of the warm and moist air was the surface heat flux over the cloud-free area to the south of the front in the daytime. While this study revealed a strong impact of land-surface heating on the nocturnal evolution of the rainband, it is necessary to keep in mind that this evolution occurred under the large influence of a strong synoptic flow, such as the westerly trough, described in the previous section. The meridional convergence between the synoptic-

CNTL (FINE)
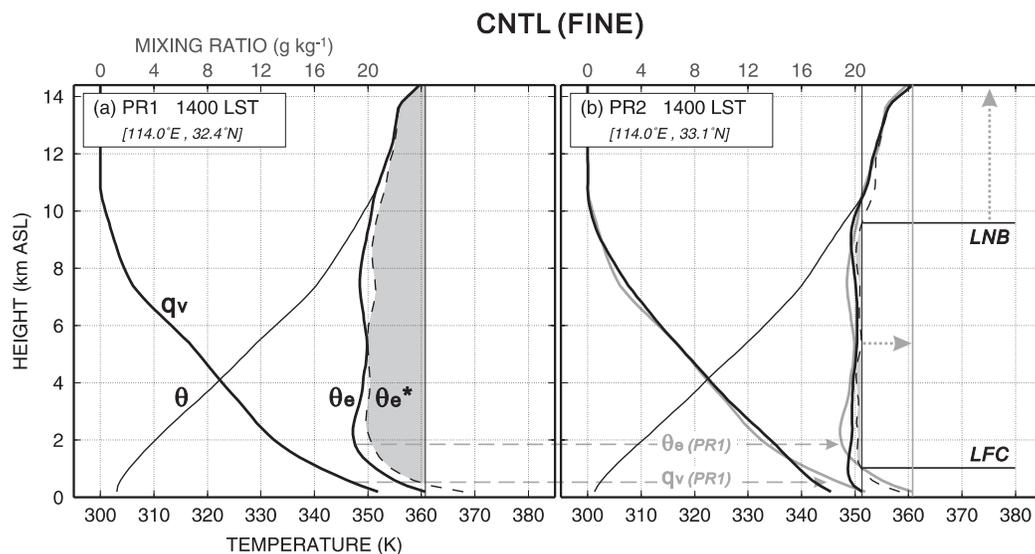
Fig. 11.   Vertical profiles of qv, θ, θ_e, and θ_e^* at PR1 and PR2 shown in Fig. 9.
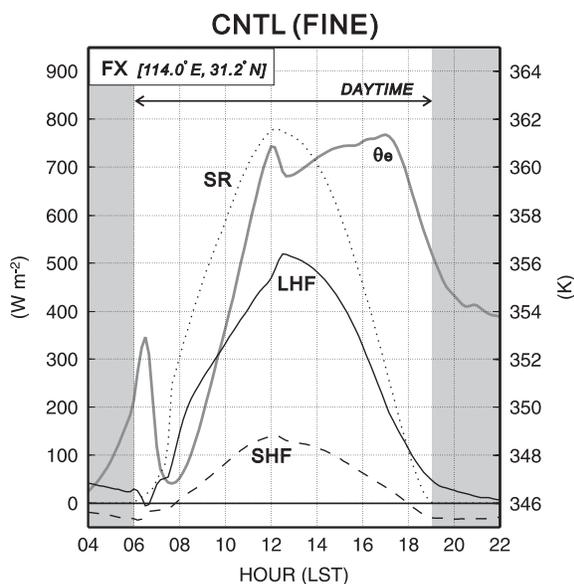
Fig. 12. Time series of the sensible and latent heat fluxes (SHF, LHF), downward shortwave radiation (SR), and equivalent potential temperature (θ_e) at FX shown in Fig. 9.

scale southerly and the northerly inflows over the front may affect rainband evolution. To examine the importance of the synoptic-scale flow, the results of a sensitivity experiment without insolation are described in the next section.

5. Sensitivity study

In CReSS, the net solar radiation absorbed by the land surface is calculated from the following equation,

$$RS \downarrow = (1 - A_l)S \downarrow (1 - 0.7CD_L)(1 - 0.6CD_M)$$
$$\times (1 - 0.3CD_H) \qquad (1)$$

where A_l is the albedo, $S \downarrow$ is the surface-level insolation under cloud-free conditions, and CD_L, CD_M, and CD_H, are the effects of scattering and absorption due to clouds in the lower, middle, and upper troposphere, respectively. A sensitivity simulation without solar radiation (hereafter "NoSR" simulation) can be accomplished by altering this equation as follows,

$$RS \downarrow = 0. \qquad (2)$$

This means that diurnal heating effects can be completely excluded while both boundary-layer and surface physical processes can be considered in the same way as in the control simulations. The convective rainband should also be reproduced in NoSR experiment if the convergence over the front was the most principal factor for the rainband evolution.

The results of NoSR experiment at 2000 LST are shown in Fig. 13. The rainfall distribution in the coarse-mesh domain (Fig. 13a) shows differences in the reproducibility between two rainfall areas near and behind the
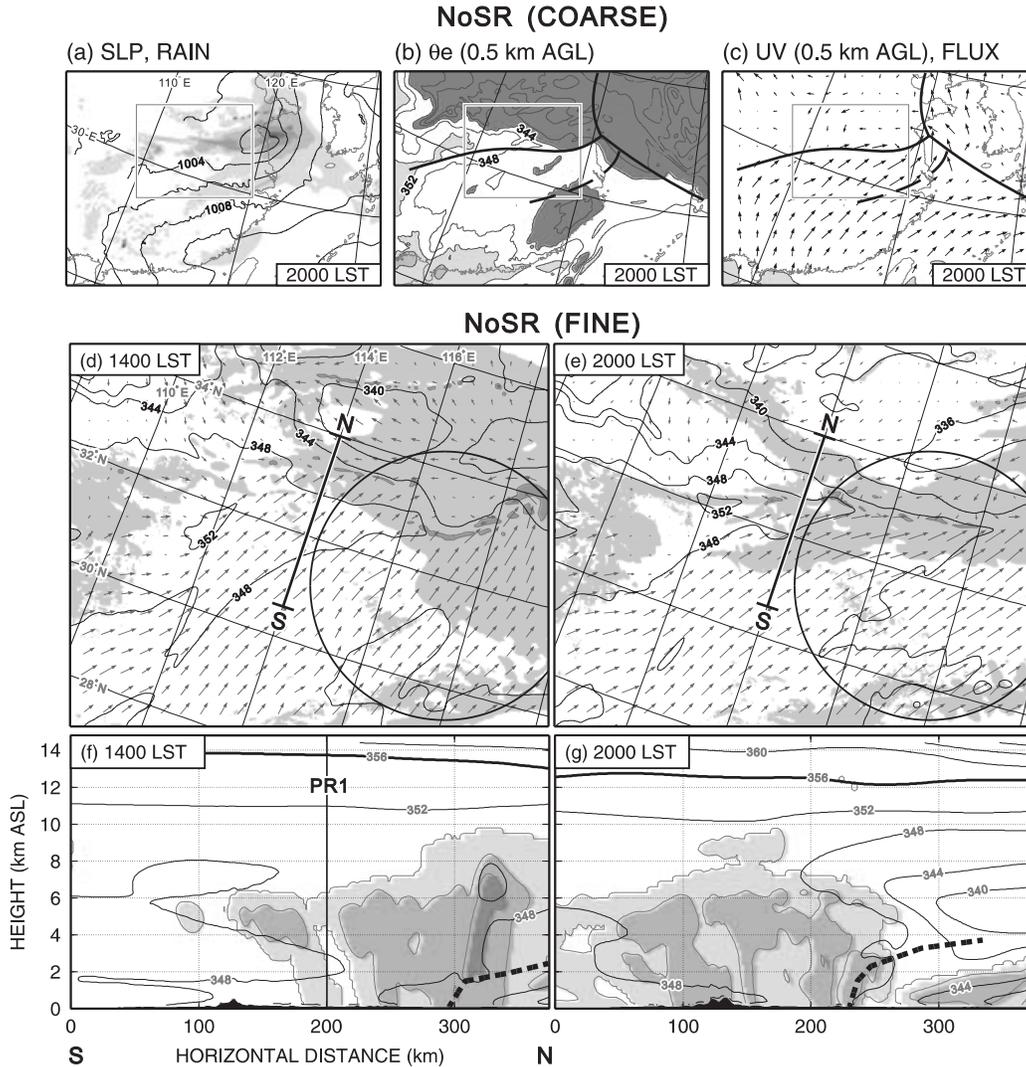
Fig. 13. Results of the experiment with no solar radiation (NoSR). (a–c) The same variables in the same form as in Fig. 6, (d and e) Fig. 7, and (f and g) Fig. 9.

depression center. Although the wide and weak rain near the depression center was reproduced almost perfectly, the rainfall intensity in the trailing rainband was much weaker than that in the control experiment (Fig. 6a). The decline in the rainband evolution was related with the lack of high-θ_e area (Fig. 13b) and surface heat flux (Fig. 13c), which is described later using the fine-mesh results. The overall distribution of the vapor flux (Fig. 13c), characterized by the strong convergence near the depression center, shows similarity to those in the control simulation. This suggests that the synoptic-scale moisture convergence

was a primary factor for the rainfall near the depression center.

The fine-mesh NoSR experiment also indicates the difference in the reproducibility between the two rainfall areas. The horizontal and vertical distributions of the wide and weak rainfall area at 1400 LST (Figs. 13d and f) are quite similar to those in the control simulation (Figs. 7a and 9b), except for the lack of high-θ_e areas. On the other hand, the distributions at 2000 LST show poor reproducibility of the trailing rainband in the NoSR experiment. In the horizontal distribution (Fig. 13e), the rainfall intensity was weak (≤ 2.0 g kg^{-1}), and the
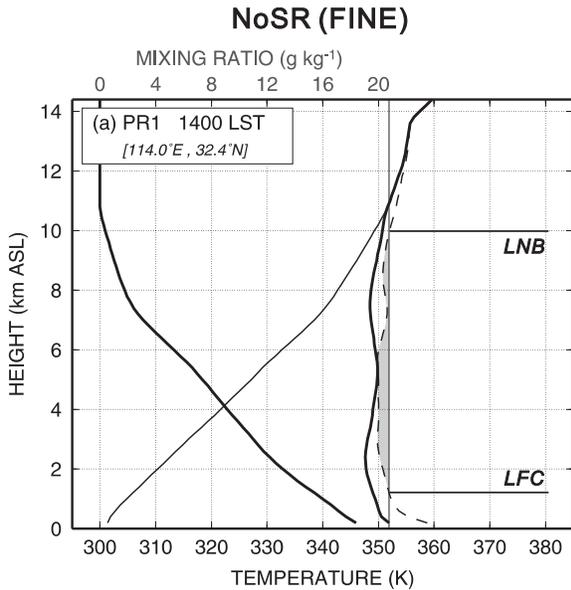
Fig. 14. The same as Fig. 11a but show-
ing the result of the NoSR experiment.

Fig. 15. Comparison of the meridional
wind component along the S–N line
(shown in Figs. 7c and 13e) above
0.8 km ASL.

width exceeding 100 km was larger than that
in the observation (Fig. 3b) and the control
simulation (<100 km, Fig. 7c). The northerly
inflow on the northern side of the rainband
was hardly reinforced, while it was reinforced
in the control simulation. The vertical section
along the S–N line (Fig. 13g) decisively indi-
cated that the NoSR experiment failed to re-
produce the deep convective updrafts of the
rainband; the depth of the cloud was limited
within 10 km ASL. The vertical thermody-
namic profile at PR1 at 1400 LST (Fig. 14)
shows that the failure of the rainband repro-
duction resulted from the weak latent instabil-
ity (139 m^2 s^{-2} of CAPE) with LNB at 10 km
ASL, indicating weaker instability than the
control simulation (Fig. 11a). It is clear that
the weak instability was strongly related to
the θ_e below 1 km ASL (352 K), which did not
rise due to the lack of land-surface heating.

The lack of high-θ_e air caused not only weak
rainband evolution but also weak frontal con-
vergence in the lower troposphere. As described
above, the strength of the northerly inflow was
quite different between the control and NoSR
experiments. This difference is emphasized by
comparing the meridional wind component
along the S–N line at 2000 LST (Fig. 15). The
wind component in the control experiment is

characterized by sharper changes, owing to
stronger southerly and northerly inflows, than
those reproduced in the NoSR experiment. This
reflects a feedback effect of the strong convec-
tive updraft on the enhancement of frontal con-
vergence, as discussed in Kato (1998). Thus,
the gradual change in the NoSR experiment re-
flects a lack of feedback due to a weak updraft.
The importance of the feedback effect for the
maintenance of the rainband is further de-
scribed in the next section.

In summary, the NoSR experiment failed to
reproduce deep updrafts and, therefore, demon-
strated the importance of the heated land sur-
face for the evolution of the rainband. This re-
sult suggests that the deep convective updrafts
of the rainband could have not been formed
without strong latent instability due to the
surface heating, even if low-level convergence
was present over a front. The other point to em-
phasize is the slight effect of surface heating on
the development of the wide and weak rainfall
near the depression center, which was well re-
produced even in the NoSR experiment. The
relative importance of the land-surface mois-
ture supply and synoptic-scale moisture con-
vergence for the two rainfall areas is quan-
titatively examined using the water budget
analysis.

6. Water budget

The budget of total water, including all water
substances and vapor, was estimated using the

(a) CNTL (b) NoSR
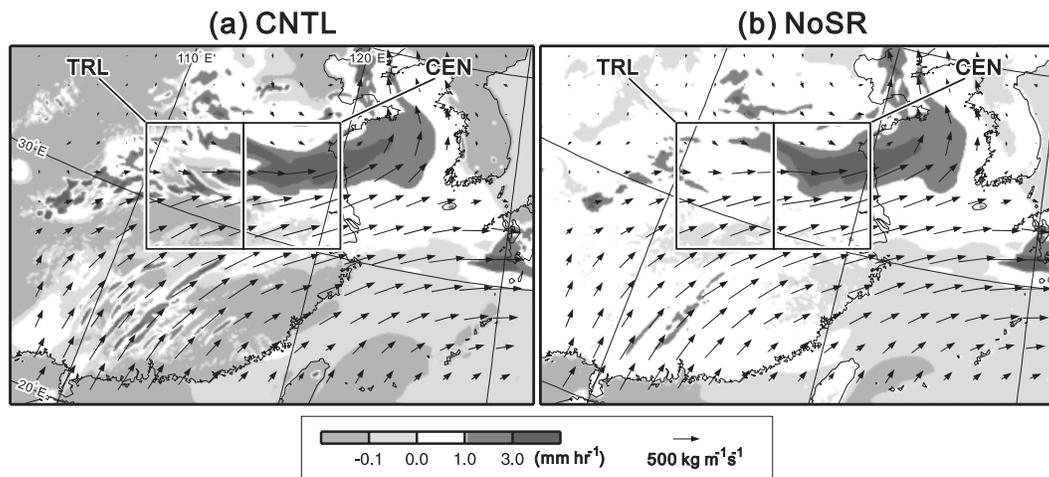
Fig. 16. Horizontal distribution of the precipitation-evaporation balance ($P - E$, shades) and vertically-integrated total water flux vectors averaged for 24 hours from 06 LST 22 June. Two rectangles are the domain of the water budget analysis: the rainfall areas near the depression center (CEN) and in the trailing portion (TRL). (a) Results of the control experiment and (b) sensitivity tests with no solar radiation.

conservation equation of the vertically integrated water amount, written as follows,

$$q_w = q_v + (q_c + q_r + q_i + q_s + q_g) \qquad (3)$$

$$\int \rho_d \left[\frac{\partial q_w}{\partial t} + \frac{\partial}{\partial x}(uq_w) + \frac{\partial}{\partial y}(vq_w) \right] dz \\ + (P - E) = 0 \qquad (4)$$

where q_w is the total water mixing ratio, P is the precipitation amount at the surface, and E is the amount of evaporation from the surface. Equation (4) consists of the terms of local change (hereafter LC), horizontal divergence (DIV), and surface-level water balance ($P - E$). DIV only consists of horizontal terms because a vertical term was counterbalanced by the vertical integration from the bottom through the top of model domain. Water budget analyses were performed using the coarse-mesh simulation results within two rectangular domains surrounding the two rainfall areas. Figure 16 shows the location of the domains, as well as the distributions of $P - E$ accumulated for 24 hours in the control and NoSR experiments. The size of the two calculation domains was 500 and 600 km in zonal and meridional directions, respectively. It is clear that these $P - E$ distributions are quite different in the trailing

portion (hereafter TRL area), while the difference is small in the area near the depression center (CEN area).

Figure 17 shows changes with time in the vertically integrated total amount of water, precipitation, evaporation, and individual terms of Eq. (4). In the TRL area of the control experiment (Fig. 17a), the total amount of water increased in the daytime (9–15 LST) and decreased during the development of the rainband (15–24 LST). It is clear that evaporation ($-E$) was responsible for this increase (i.e., a positive LC value in 09–14 LST). As seen in the horizontal distribution (Fig. 16a), evaporation (negative value of $P - E$) was predominant in the southern half of the TRL area. During the rainband evolution, the decrease in the total water and negative LC were almost balanced with a positive $P - E$ value, which indicates that the rainband developed by consuming water vapor accumulated in the TRL area. This supports the primary importance of evaporation from the continental surface for the rainband evolution. In contrast, the value of moisture divergence (DIV) was small throughout the analysis period, owing to the offset of convergence in the meridional direction against zonal divergence, as seen in the flux vectors in Fig. 16a. Nonetheless, in Fig. 17a,
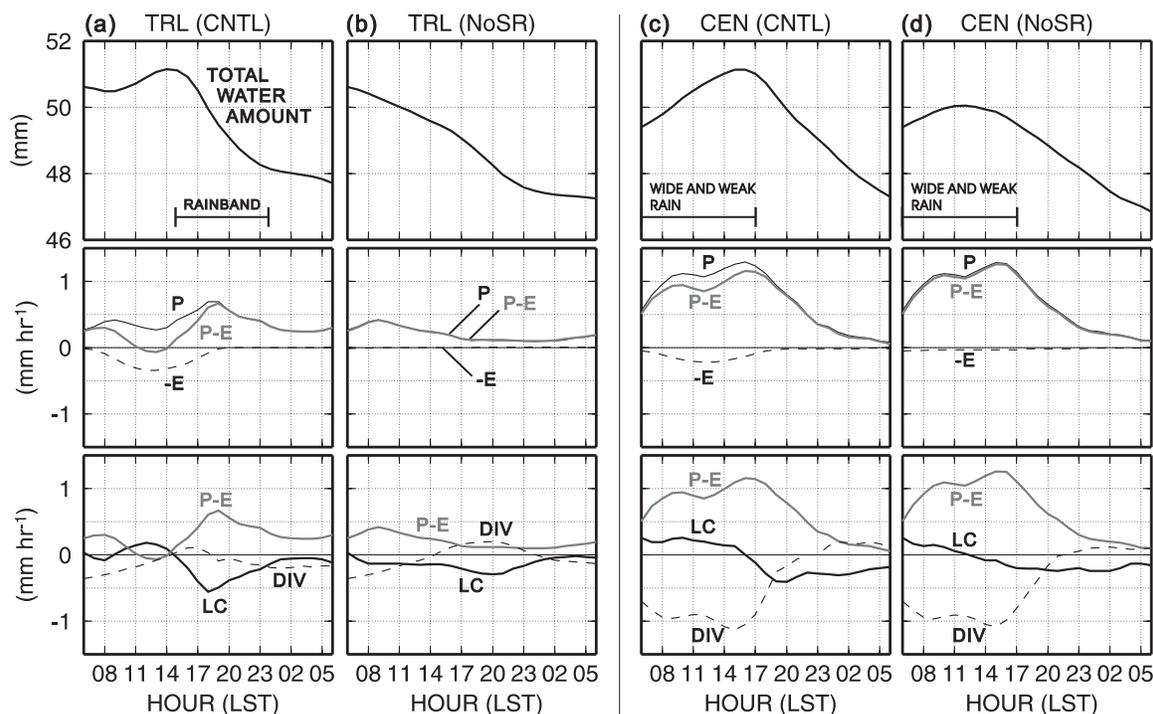
Fig. 17. (a and b) Change with time in the total amount of water, precipitation (P), evaporation ($-E$), precipitation-evaporation balance ($P - E$), and terms in Eq. (4), calculated within the TRL area of the control and the NoSR experiments. (c and d) The same but within the CEN area.

the weak convergence after midnight (00–06 LST) contributed to the maintenance of rainfall (positive $P - E$). The increase in the convergence is the manifestation of the rainband's feedback effect, described in the previous section. The budget of NoSR experiment (Fig. 17b) shows a very different time series from that of the control. The lack of evaporation and total water increase in the daytime did not lead to rainfall evolution in the night and its feedback effect in the late night.

In contrast, the water budget in the CEN area of the control experiment (Fig. 17c) clearly indicates the primary importance of convergence for precipitation. $P - E$ was roughly balanced with DIV until 18 LST, that is, in the period that the wide and weak rainfall area was predominant over the CEN area. Although the value of evaporation was not small (-0.2 mm hr^{-1} in largest), its contribution to precipitation (up to 1.3 mm hr^{-1}) was relatively smaller than that of the convergence (-1.1 mm hr^{-1}). The balance of $P - E$ with

DIV is also evident in the budget of the NoSR experiment (Fig. 17d). These results indicate that the impact of evaporation was secondary on the rainfall evolution near the depression center.

These results, therefore, suggest that the impact of land-surface moisture supply on the rainfall evolution may vary according to the synoptic-scale flow features. Under a strong effect of the synoptic-scale flow, since low-level convergence and upward lifting of water vapor are mainly responsible for precipitation, the effect of evaporation should be relatively small. In other words, evaporation has a potential to be the primary factor causing rainfall out of the synoptic-scale updraft areas. It is known that cloud clusters can develop over a Meiyu front, even under a situation with no upper-level trough (e.g., Ninomiya and Shibagaki 2003; Maesaka and Uyeda 2006a). The impact of land-surface evaporation on such cloud clusters remains to be investigated in further studies.
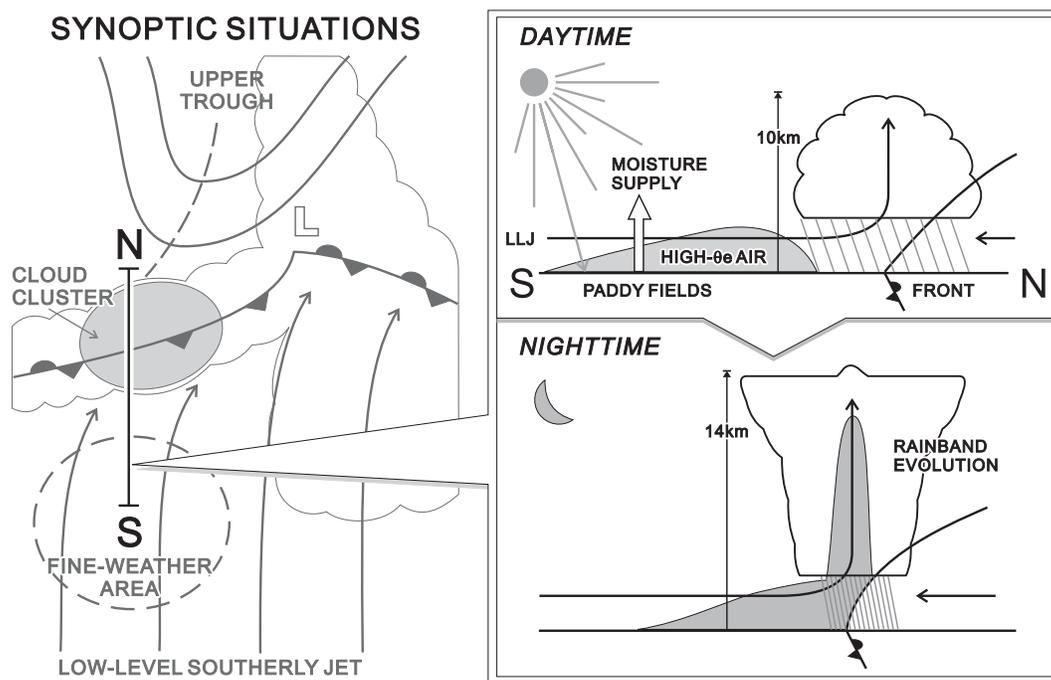
Fig. 18.   Schematic view of the relationship between the formation of high-θ_e air and the evolution of
the deep convective rainband in the trailing part of a depression along a Meiyu-Baiu front.

7.   Conceptual model

From the results of this study, a conceptual
model on the effect of the heated continent on
the evolution of a cloud cluster can be pro-
posed, as illustrated in Fig. 18. This cloud clus-
ter was formed in the trailing portion of a
Meiyu frontal depression that developed under
the influence of a westerly trough in the upper
troposphere. The synoptic-scale situations of
the cluster were characterized by a strong
southerly inflow in the lower troposphere. A
rainband with deep convective updrafts, corre-
sponding to the cloud cluster, started to develop
in the late afternoon and remained in the
night. Before the evolution, the continental
land surface, mostly reclaimed as paddy fields,
was heated by insolation in a cloud-free area
to the south of the frontal zone. High-θ_e air
formed near the surface due to the supply of la-
tent heat (i.e., moisture), and was transported
northward by a low-level southerly jet. The hor-
izontal transport of high-θ_e air in the lower tro-
posphere caused strong latent instability over
the front. The uplift of high-θ_e air, due to the

frontal convergence, brought the deep convec-
tive updrafts of the rainband that remained
while high-θ_e air was fed. This conceptual
model, therefore, clearly indicates a strong im-
pact of the continental surface, heated by inso-
lation, upon the evolution of deep convective
cloud systems over a Meiyu front, especially at
night.

8.   Summary and discussion

Numerical simulations of a rainband, corre-
sponding to a cloud cluster over a Meiyu front,
were conducted in this study, to demonstrate
the thermodynamic impact of the mainland
China, heated by insolation, upon the evolution
of the rainband. The Nagoya University Cloud
Resolving Storm Simulator (CReSS) was used
to reproduce the rainband evolution without
any convective parameterization scheme. The
simulations were conducted within doubly
nested domains with coarse (5 km) and fine
(2 km) horizontal grid spacing. The domain of
the coarse-mesh grids covered the plains and
hills in eastern and southern China, to repro-
duce the land-surface heating process to the

south of the front. The land-surface conditions were initiated homogeneously by assuming a land use of primarily paddy fields, according to the results of past studies. The observational and reanalysis data were used to describe the mesoscale feature of the deep convective clouds and to examine the reality of simulation results.

A cloud cluster, the object of the simulation, developed in the rear of a Meiyu frontal depression in the late afternoon of 22 June 2003, and remained in the night. Data collected in the intensive field experiment revealed the mesoscale characteristics of the cloud cluster, that is, an organized rainband with a high cloud shield and latently unstable thermodynamic stratification due to a southerly inflow with θ_e higher than 356 K in the lower troposphere. The reanalysis data showed a synoptic-scale environment characterized by the evolution of a frontal depression under the influence of an upper-level westerly trough and a low-level southerly inflow. The reanalysis data also suggested that the low-level southerly inflow was heated and moistened in the daytime over the continent, and was responsible for the rapid extension of the high-θ_e area to the south of the front.

A control simulation reproduced the evolution of the rainband without contradicting the observational evidence reported above. This simulation showed that the rainband evolution resulted from the strong latent instability over the front, which was caused by the southerly inflow of the high-θ_e air. The origin of high-θ_e air was mainly latent heat flux from the land surface over the cloud-free area to the south of the front in the daytime. The moist surface, corresponding to the paddy fields, was responsible for the moisture supply. The sensitivity simulation without insolation failed in reproducing deep convective updraft of the rainband and, therefore, proved the importance of the surface heating for the rainband evolution. The water budget analysis within the area surrounding the rainband demonstrated the importance of the land-surface evaporation rather than horizontal moisture convergence for the rainband evolution.

These results lead to the conclusion that the continental land surface heated by insolation has a significant impact upon the evolution of a cloud cluster over a Meiyu front. It is important to note that the diurnal heating affected the evolution of the cluster even during the night. This delay (more than 6 hours) can be explained by horizontal wind speed in the lower troposphere (about $14 \mathrm{~ms^{-1}}$) and the distance between the cloud-free area and front (300 km). This suggests that a synoptic-scale strong southerly inflow in the lower troposphere was also an important background for the moisture transport, low-level convergence over the front, and rainband evolution.

Although this study has clarified the importance of land-surface heating from a case study, there is room for argument on the generality. As revealed through water budget analysis, the impact of land-surface moisture supply on the rainfall evolution may vary according to the synoptic-scale flow features. Since cloud clusters can develop over a Meiyu front even under various synoptic-scale conditions, more case studies and a statistical approach are needed to solve this issue. In addition, it is necessary to verify the relative importance of the land-surface heating to other factors (e.g., destabilization, due to differential horizontal advection, Ninomiya and Shibagaki 2003), through further researches using various kinds of reanalysis data and numerical models. The importance of the other factors in initial conditions largely depends on the accuracy of the reanalysis data. Nevertheless, it must be emphasized that the land-surface heating has a potential to be a crucial factor in the nocturnal evolution of mesoscale convective systems and MCCs over the landmass.

Another direction for research based on this study would be the impact of land-surface conditions for the various mesoscale structures of convective cloud systems. The vertical structure of convective systems over a Meiyu frontal zone, with a peak of radar reflectivity near 3 km and a rapid decrease above the melting layer (Zhang et al. 2006), is quite different from that over the Great Plains (Zipser and Lutz 1994). It is possible that different vertical structures reflect the differences in primary land use, namely, paddy fields over China, compared with wheat fields and grasslands over the Great Plains of the US. Surface conditions, such as soil moisture and evapotranspiration efficiency, can affect the rate of sensible to la-

tent heat flux, and may control the boundary-layer conditions. Yamada and Uyeda (2006) and Yamada (2007) clarified a significant impact of the land surface conditions upon the convective structure and precipitation process over the Tibetan Plateau in summer. While the use of a coupled mesoscale atmosphere-land surface model (e.g., Trier et al. 2004) becomes important to reproduce cloud development more accurately, idealized simulations using homogeneous land-use categories will also be useful to understand the dependency of convective structure on land-surface conditions.

Acknowledgments

References

Anderson, C.J. and R.W. Arritt, 1998: Mesoscale convective complexes and persisted elongated convective systems over the United States during 1992 and 1993. *Mon. Wea. Rev.*, **126**, 578–599.

Chen, C.-S., 1991: A numerical study of a squall line over the Taiwan Strait during TAMEX IOP 2 events. *Mon. Wea. Rev.*, **119**, 2677–2698.

Chen, S.-J., Y.-H. Kuo, W. Wang, Z.-Y. Tao, and B. Cui, 1998: A modeling case study of heavy rainstorms along the Meiyu front. *Mon. Wea. Rev.*, **126**, 2330–2351.

Chen, G.T.-J., C.-C. Wang, and D.T.-W. Lin, 2005: Characteristics of low-level jets over northern Taiwan in Mei-Yu season and their relationship to heavy rain events. *Mon. Wea. Rev.*, **133**, 20–43.

Geng, B., H. Yamada, K.K. Reddy, H. Uyeda, and Y. Fujiyoshi, 2004: An observational study of the development of a rainband on a Meiyu front causing heavy rainfall in the downstream region of the Yangtze River. *J. Meteor. Soc. Japan*, **82**, 1095–1115.

Hu, G. and Y. Ding, 2006: Yangtze River flood in 1998: water vapor cycle. *Final Report of GAME-HUBEX—GEWEX Asian Monsoon Experiment/Huaihe River Basin Experiment—(GAME Publication No. 43)*, 104–126.

Ikebuchi, S., M. Shiiba, Y. Tachikawa, and K. Tanaka, 1998: Observation and modeling of land-surface fluxes in HUBEX. *Preliminary research report on Japanese GAME/HUBEX*, 364–388.

Ishihara, M., Y. Fujiyoshi, A. Tabata, H. Sakakibara, K. Akaeda, and H. Okamura, 1995: Dual Doppler radar analysis of an intense mesoscale rainband generated along the Baiu front in 1988: Its kinematical structure and maintenance process. *J. Meteor. Soc. Japan*, **73**, 139–163.

Iwasaki, H. and T. Takeda, 1993: Characteristic features on meso-scale cloud clusters around Japan in the Baiu-season from 1985 to 1988. *Tenki*, **40**, 161–170 (in Japanese).

Kato, T., 1998: Numerical simulation of the band-shaped torrential rain observed over southern Kyushu, Japan on 1 August 1993. *J. Meteor. Soc. Japan*, **76**, 97–128.

Laing, A.G. and J.M. Fritsch, 1997: The global population of mesoscale convective complexes. *Quart. J. Roy. Meteor. Soc.*, **123**, 389–405.

Li, J., Y.L. Chen, and W.C. Lee, 1997: Analysis of a heavy rainfall event during TAMEX. *Mon. Wea. Rev.*, **125**, 1060–1082.

Li, Z., T. Takeda, K. Tsuboki, K. Kato, M. Kawashima, and Y. Fujiyoshi, 2007: Nocturnal evolution of cloud clusters over eastern China during the intensive observation periods of GAME/HUBEX. *J. Meteor. Soc. Japan*, **85**, 25–45.

Maesaka, T. and H. Uyeda, 2006a: Development processes of precipitation systems on 29–30 June and 2–3 July 1998. *Final Report of GAME-HUBEX—GEWEX Asian Monsoon Experiment/Huaihe River Basin Experiment—(GAME Publication No. 43)*, 329–382.

Maesaka, T. and H. Uyeda, 2006b: Synoptic and meso-α-scale disturbances: general description for 1998 IOP. *Final Report of GAME-HUBEX—GEWEX Asian Monsoon Experiment/Huaihe River Basin Experiment—(GAME Publication No. 43)*, 145–153.

Moteki, Q., H. Uyeda, T. Maesaka, T. Shinoda, M. Yoshizaki, and T. Kato, 2004: Structure and development of two merged rainbands observed over the East China Sea during X-BAIU-99. Part I: Meso-β-scale structure and development processes. *J. Meteor. Soc. Japan*, **82**, 19–44.

Ninomiya, K., 1999: Moisture balance over China and the South China Sea during the summer monsoon in 1991 in relation to the intense rainfalls in China. *J. Meteor. Soc. Japan*, **77**, 737–751.

Ninomiya, K., 2001: Large λ-shaped cloud zone formed around July 6, 1991 with pole-ward

moisture transport from intense rainfall area in Meiyu–Baiu front. *J. Meteor. Soc. Japan*, **79**, 805–813.

Ninomiya, K. and C. Kobayashi, 1992: Precipitation and moisture balance of the Asian summer monsoon in 1991. Part II: Moisture transport and moisture balance. *J. Meteor. Soc. Japan*, **77**, 77–99.

Ninomiya, K. and Y. Shibagaki, 2003: Cloud system families in the Meiyu-Baiu front Observed during 1–10 July 1991. *J. Meteor. Soc. Japan*, **81**, 193–209.

Reynolds, R., N. Rayner, T. Smith, D. Stokes, and W. Wang, 2002: An improved in-situ and satellite SST analysis for Climate. *J. Climate*, **15**, 1609–1625.

Segami, A., K. Kurihara, H. Nakamura, M. Ueno, I. Takano, and Y. Tatsumi, 1989: Operational mesoscale weather prediction with Japan Spectral Model. *J. Meteor. Soc. Japan*, **67**, 907–924.

Shin, C.-S. and T.-Y. Lee, 2005: Development mechanisms for the heavy rainfalls of 6–7 August 2002 over the middle of the Korean Peninsula. *J. Meteor. Soc. Japan*, **83**, 683–709.

Shinoda, T. and H. Uyeda, 2002: Effective factors in the development of deep convective clouds over the wet region of Eastern China during the summer monsoon season. *J. Meteor. Soc. Japan*, **80**, 1395–1414.

Shinoda, T., H. Uyeda, and K. Yoshimura, 2005: Structure of moist layer and sources of water over the southern region far from the Meiyu/Baiu front. *J. Meteor. Soc. Japan*, **83**, 137–152.

Trier, S.B., F. Chen, and K.W. Manning, 2004: A study of convection initiation in a mesoscale model using high-resolution land surface initial conditions. *Mon. Wea. Rev.*, **132**, 2954–2976.

Tsuboki, K. and A. Sakakibara, 2002: *Large-scale parallel computing of cloud resolving storm simulator*. High Performance Computing, H.P. Zima et al., Eds., Springer, 243–259, http://www.rain.hyarc.nagoya-u.ac.jp/~tsuboki/src/pdf_research/ishpc2002_tsuboki.pdf.

Wang, C.-C., G.T.-J. Chen, T.-J. Chen, and K. Tsuboki, 2005: A numerical study on the effects of Taiwan topography on a convective line during the Mei-Yu season. *Mon. Wea. Rev.*, **133**, 3217–3242.

Yamada, H., 2007: Numerical simulations of the role of land-surface conditions in the evolution and structure of summertime thunderstorms over a flat highland. *Mon. Wea. Rev.*, **135** (in press).

Yamada, H. and H. Uyeda, 2006: Transition of the rainfall characteristics related to the moistening of the land surface over the central Tibetan Plateau during the summer of 1998. *Mon. Wea. Rev.*, **134**, 3230–3247.

Yamada, H., B. Geng, K.K. Reddy, H. Uyeda, and Y. Fujiyoshi, 2003: Three-dimensional structure of a mesoscale convective system in a Baiu-frontal depression generated in the downstream region of the Yangtze River. *J. Meteor. Soc. Japan*, **81**, 1243–1271.

Yamasaki, M., 2002: A study of cloud clusters associated with a Baiu front by use of a mesoscale-convection-resolving model. *J. Meteor. Soc. Japan*, **80**, 595–619.

Yamasaki, M., 2005: A numerical study of cloud clusters and a meso-α-scale low associated with a Meiyu front. *J. Meteor. Soc. Japan*, **83**, 305–329.

Zhang, C.-Z., H. Uyeda, H. Yamada, B. Geng, and Y. Ni, 2006: Characteristics of mesoscale convective systems over the east part of continental China during the Meiyu from 2001 to 2003. *J. Meteor. Soc. Japan*, **84**, 763–782.

Zipser, E.J. and K.R. Lutz, 1994: The vertical profile of radar reflectivity of convective cells: A strong indicator of storm intensity and lightning probability? *Mon. Wea. Rev.*, **122**, 1751–1759.